

# The Role of Stress Distribution in Seismic Cycle Complexity: Evidence from Long Laboratory Fault Experiments

F. Paglialunga<sup>1</sup>, F. Passelègue<sup>1</sup>, JP. Ampuero<sup>1</sup>, S. Latour<sup>2</sup>, M. Violay<sup>3</sup>

<sup>1</sup>Université Côte d’Azur, CNRS, Observatoire de la Côte d’Azur, IRD, Géoazur, Sophia Antipolis, France

<sup>2</sup>Université de Toulouse, CNRS, Observatoire Midi-Pyrénées, IRAP, Toulouse, France

<sup>3</sup>École Polytechnique Fédérale de Lausanne, Switzerland.

## Key Points:

- Loading conditions strongly influence stress distribution and rupture nucleation location
- Heterogeneous fault stress promotes the transition from system-size to complex seismic cycles
- Heterogeneous stress influences rupture dynamics, leading to abrupt decelerations and delayed secondary rupture

---

Corresponding author: F. Paglialunga, [federica.paglialunga@geoazur.unice.fr](mailto:federica.paglialunga@geoazur.unice.fr)

## Abstract

A fundamental understanding of the factors controlling the complexity of seismic cycles is crucial to advance the study of earthquake hazard and predictability. Among these factors, stress distribution and fault system size play a significant role in shaping the complex patterns of seismic behavior. This study examines how heterogeneous loading conditions influence the seismic cycles of a long experimental fault. Seismic cycles are reproduced on analog material (poly methyl methacrylate) in a biaxial apparatus while continuously monitoring the strain field near the fault. By examining the effects of stress variability on fault behavior, we identify a whole spectrum of rupture outcomes, ranging from periodic, system-wide failures to complex seismic sequences comprising several partial ruptures before a complete event. Additionally, the resulting heterogeneous initial stress conditions before each event significantly influence their rupture dynamics, leading to abrupt rupture slowdown and subsequent delayed renucleation. The results provide a framework for understanding the evolution of stress heterogeneity along natural faults and its implications for earthquake predictability and rupture dynamics.

## Plain Language Summary

Earthquakes present a serious threat to our society, causing loss of life and economic damage. Understanding what controls their occurrence (i.e., the seismic cycle) is essential for effective hazard assessment. However, natural faults are difficult to study directly, and their geometry and stress conditions are often unknown. To address this, we develop an experimental study that simulates seismic activity on a long artificial fault, simplifying the system for better understanding. Using a high-frequency acquisition system, we were able to monitor the stress evolution along the fault and emphasize the importance of its distribution. In particular, heterogeneous stress along the fault was found (i) to cause complex seismic sequences, with multiple partial events occurring between major ruptures, and (ii) to strongly affect the dynamics of individual ruptures.

## 1 Introduction

Understanding the relationship between along-fault stress distribution and fault behavior is a fundamental challenge in earthquake science, with significant implications for seismic hazard assessment. Natural fault systems are controlled by many interacting factors that govern rupture nucleation, propagation, and arrest. Among these factors, initial along-fault stress distribution is a key driver of rupture dynamics, influencing the size, recurrence interval, and spatial characteristics of seismic events. Das & Aki (1977) demonstrated that a stress barrier can influence the rupture dynamics and the general complexity of slip profiles. Caniven et al. (2017) showed through an analog model how spatial variations of fault normal stress *‘control the ability of the fault to generate irregular or regular seismic cycles and produce clustering sequences’*. Such complex seismic cycles are also known as supercycles (Salditch et al., 2020).

Together with stress heterogeneity, another key aspect that contributes to the seismic cycle complexity is the system size. In particular, the ratio between the fault length  $L$  and the cohesive zone size  $L_c$  is pivotal. For large  $\frac{L}{L_c}$ , Lapusta & Rice (2003) highlighted the emergence of partial ruptures between complete events that break the whole fault, sharing similar nucleation characteristics. Cattania (2019) demonstrated that a larger ratio  $\frac{L}{L_c}$  leads to complex earthquake sequences even along planar faults with homogeneous frictional properties, when driven by the heterogeneous loading imposed by fault creep outside the seismogenic zone. The occurrence of partial events implies the arrest of a propagating rupture. This condition is favored in long fault systems (Ke et al., 2020) and is expected to be enhanced by heterogeneous stress distributions (Tinti et al., 2005; Radiguet et al., 2013, 2015; Bayart et al., 2018; S. B. Cebry et al., 2023).

However, studying the role of stress heterogeneity on seismic behavior is complicated by the fact that earthquakes typically occur at large depths. Except for rare cases (Bakun 2005, Turkey, 2023), instrumenting faults and gaining insights into their loading and geometrical conditions remains challenging. One promising solution is to replicate earthquakes on artificial faults in controlled laboratory settings equipped with advanced acquisition systems. While simplifying natural fault systems, especially their rheology and geometry, this approach allows investigation of many key aspects of seismic activity, leading to valuable insights into earthquake physics and mechanics (Brace & Byerlee, 1966; Rosakis et al., 1999; Xia et al., 2004; Lu et al., 2007; Yamashita et al., 2021a; Svetlizky & Fineberg, 2014; McLaskey & Lockner, 2014; Bayart et al., 2018; McLaskey, 2019; Rubino & Rosakis, 2020; Gvirtzman & Fineberg, 2021; Tal et al., 2022; Rubino et al., 2022a; Paglialonga et al., 2022; Mastella, 2022; S. B. Cebry et al., 2023; Corbi, 2024; Fryer et al., 2024).

Large-scale friction experiments on rocks, with artificial faults much longer than typical experimental length scales (i.e. 5-8 cm), have unveiled important features of laboratory earthquakes (Dieterich, 1978, 1981; Okubo & Dieterich, 1981, 1984; Yamashita et al., 2018, 2021b; Ke et al., 2018, 2020). However, despite their size, the ratio  $L/L_c$  in the rock samples tested so far has remained small compared to what is expected in nature. Using analog materials like polymers, which have smaller elastic moduli and critical slip distances than rocks, allows to increase the  $L/L_c$  ratio by one order of magnitude compared to rock fault interfaces (Rosakis et al., 1999; Latour et al., 2013; Svetlizky & Fineberg, 2014; Svetlizky et al., 2017; Bayart et al., 2016, 2018; Guérin-Marthe et al., 2019; Gounon et al., 2022; S. B. L. Cebry et al., 2022; Rubino et al., 2022b). In this study, we present new experimental results highlighting the influence of heterogeneous stress distributions on the seismic behavior of a long laboratory fault with  $L/L_c \sim 100$ . Our results demonstrate that a heterogeneous loading can (i) affect the nucleation location of instabilities, (ii) increase the number of partial events between two complete ruptures without changing the recurrence time of the latter, and (iii) induce complex dynamic rupture propagation processes.

## 2 Experimental setup and methods

A large biaxial apparatus containing a 2.5 m long fault was built in the Laboratory of Experimental Rock Mechanics (LEMR) at the Swiss Federal Institute of Technology of Lausanne (EPFL), allowing for a ratio of  $L/L_c \sim 100$ , so far the largest value employed for experimental studies. Under a direct single-shear configuration, two samples are pressed against each other and successively sheared to produce frictional ruptures. This experimental setup is designed to host samples of analog material with dimensions 2.5 x 0.5 x 0.03 m that can slip along an artificial interface 2.5 m long and 0.03 m thick (Figure 1a). The samples are made of polymethyl methacrylate (PMMA), characterized by S-wave velocity  $C_s = 1350$  m/s and P-wave velocity  $C_d = 2700$  m/s. The normal load is applied through twenty hydraulic pistons, organized into four distribution plates that can independently apply specific loads, enabling both homogeneous and heterogeneous normal stress distributions. The shear load is applied through five pistons moving a steel plate, uniformly distributing the stress throughout the bottom lateral side of the sample (Figure 1a). The pistons apply an elastic loading rate of around 0.44 MPa/s.

The strain evolution along the fault length was monitored through strain gauges with a recording frequency of 40 kHz, using a National Instrument system. Strain gauge rosettes were positioned close to the fault ( $\sim 3$  mm away from the fault plane) at nine locations, of which eight could be used simultaneously (Figure 1a). Stress tensors were obtained by assuming plane stress conditions (details on the stress derivation can be found in the supplementary material).

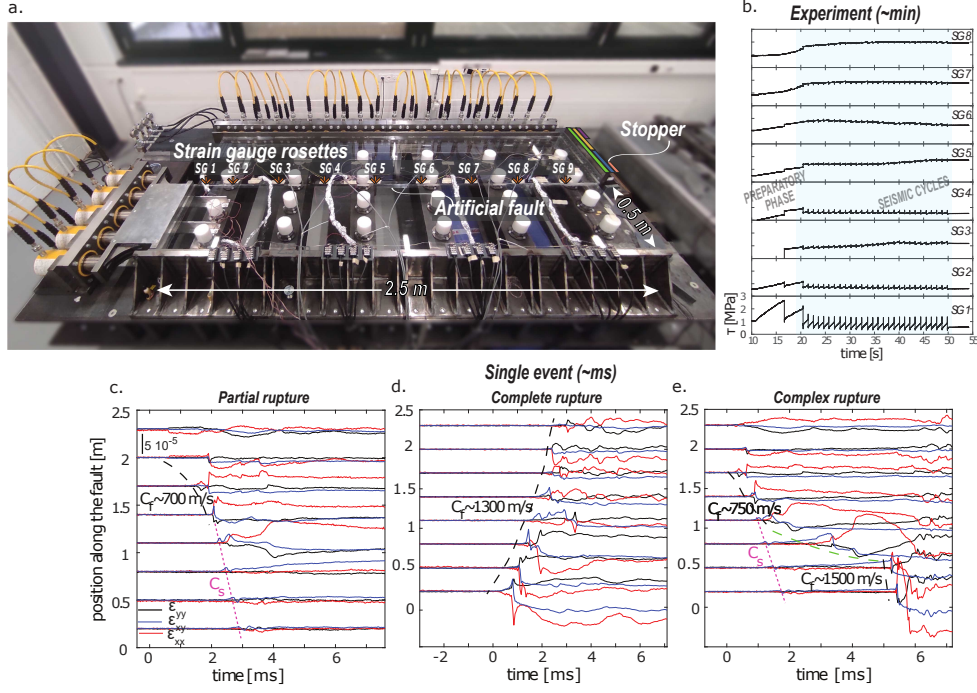


**Figure 1.** (a) Picture of the large biaxial apparatus located at LEMR-EPFL. Two PMMA samples are loaded through pistons applying both normal and shear stress. Strain gauge rosettes are located along the fault length around 3 mm away from the fault plane. Different stoppers were used in this study, each indicated by a different color, with the same legend throughout the manuscript. (b) Temporal evolution of shear stress ( $\tau$ ) throughout 8 different experiments. Data recorded during typical examples of laboratory earthquakes: (c) partial event, (d) complete event, (e) complex event. Black dashed lines indicate the dynamic rupture propagation, purple dotted curves indicate S-wave velocity and green dashed curves indicate strain transfer.

Five different stopper configurations were used in the experiments (Figure 1a) to modify the external loading (Iwashita et al., 2023), thereby influencing the stress loading distribution along the fault. The first configuration used a stopper 50 cm long, spanning the entire height of the sample. This configuration is referred to as the “large stopper” and is indicated in green. The second and third configurations utilized a 20 cm-long stopper placed, respectively, at 28 cm (referred to as the “top-medium stopper”, shown in yellow) and at 9 cm from the fault plane (referred to as the “bottom-medium stopper”, shown in blue). The fourth and fifth configurations involved an 8.5 cm-long stopper positioned, respectively, at 38 cm (referred to as the “top-small stopper”, shown in purple) and 9 cm from the fault plane (referred to as the “bottom-small stopper”, shown in orange).

### 3 Results

#### 3.1 Laboratory earthquakes

Across all experiments conducted, the overall fault behavior exhibited characteristics that are typically observed in biaxial experimental setups. During the application of shear load, the shear stress along the fault increased correspondingly. After a “preparatory phase” involving partial rupture events (Rubinstein et al., 2004; Kammer et al., 2015) (Figure 1b), a sequence of recurrent seismic cycles started, including ruptures that propagated along the entire fault length.

Three principal types of dynamic events were identified using the strain gauges along the fault: partial ruptures (Figure 1c), complete ruptures (Figure 1d), and complex ruptures (Figure 1e). Partial ruptures predominantly nucleated on the right side of the fault (near  $x=2.3$  m), where they accelerated into a dynamic propagation phase (indicated by dashed black lines). These ruptures reached a speed of approximately  $\sim 700$  m/s ( $\simeq 0.52C_s$ ), then decelerated and arrested without reaching the edge of the sample. This arrest induced localized strain accumulation in the regions that did not rupture (Figure 1c). In the complete rupture example (Figure 1d), the rupture nucleated at the left edge of the fault ( $x=0$  m) and dynamically propagated across the entire fault length with an average rupture velocity of  $\sim 1250$  m/s ( $\sim C_r$ ). However, the majority of complete ruptures exhibited complex dynamics (Figure 1e). These events, referred to as complex ruptures, generally nucleated near  $x=2.3$  m, and promptly accelerated to a speed of  $\sim 750$  m/s. The rupture front was subsequently halted at position  $x=1.1$  m, resulting in a slow but continuous strain accumulation over a 0.5 m segment of the fault. The rupture then re-nucleated and propagated through the remaining portion of the fault at supershear velocity ( $\sim 1500$  m/s).

#### 3.2 Influence of initial stress distribution on rupture nucleation

The nucleation location of complete ruptures was determined and analyzed for each experiment in relation to the stress distribution along the fault. We focused on complete ruptures, as partial ones consistently nucleated on the same portion of the fault (right side) coherently with previous laboratory observations that have been already largely studied (Rubinstein et al., 2011; Kammer et al., 2015). The distributions of the ratio  $\frac{\tau}{\sigma_{yy}}$  before each rupture event, quadratically interpolated between the strain gauges, are shown by the gray solid lines in Figure 2.

Our experimental results confirm that the external boundary conditions control the rupture nucleation locations. Ruptures nucleated near either the right or left edge of the fault (histogram in Figure 2). When the large or the top-small stopper was employed, all ruptures consistently nucleated on the right side (Figures 2a, e). Notably, with the top-small stopper, the average nucleation location shifted slightly toward the central part of the fault (Figure 2e). In contrast, other stopper configurations resulted in nucleation

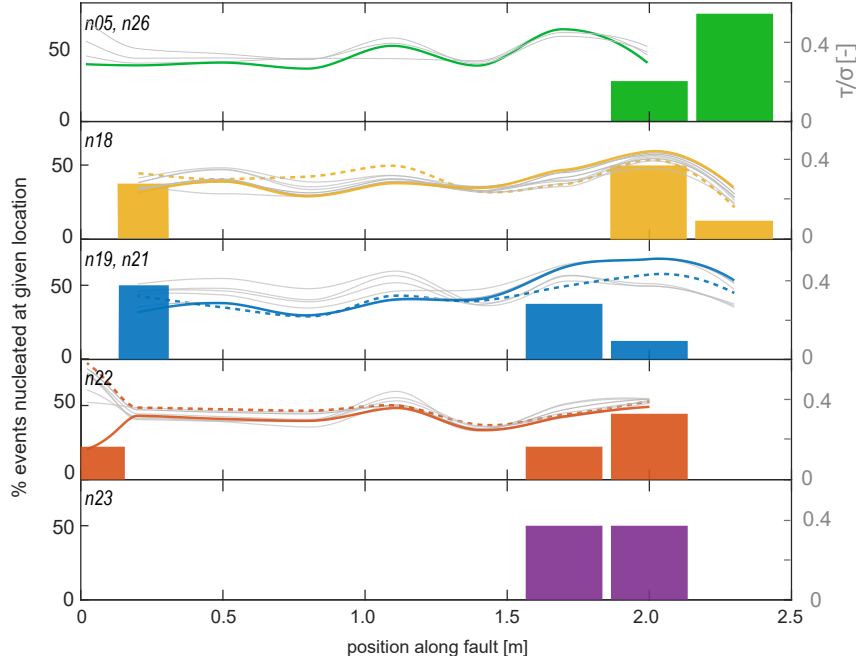


**Figure 2.** Distribution of event nucleation locations along the fault for the different initial boundary conditions. The colors refer to experiments with different stoppers indicated in Figure 1. Curves show distributions of  $\frac{\tau}{\sigma_{yy}}$  before each event for all events studied (gray) and before selected ruptures nucleating on the right side of the fault (colored solid lines) and on the left side (colored dashed lines).

occurring on both the left and right sides (Figures 2b-d). For the top-medium stopper, 62% of the events nucleated on the right side, while 38% occurred on the left. The bottom-medium stopper exhibited the most balanced distribution, with nearly 50% of events nucleating on each side of the fault. Lastly, the bottom-small stopper predominantly induced nucleation on the right side, with only 22% of complete ruptures originating on the left.

A representative friction profile recorded before an event nucleating on the right (left) side is shown as solid (dashed) colored lines. At first order, the nucleation occurs where  $\frac{\tau}{\sigma_{yy}}$  reaches its largest value. For example, right-side nucleation events coincided with the highest  $\frac{\tau}{\sigma_{yy}}$  values, measured as 0.41, 0.44, 0.52, and 0.38 for the large stopper, top-medium stopper, bottom-medium stopper, and top-small stopper, respectively (solid colored lines, Figures 2a-d). This trend was confirmed for events nucleating on the left side in experiments where strain gauge data were available on that portion of the fault. For instance, with the top-small stopper configuration, left-side ruptures nucleated at a local  $\frac{\tau}{\sigma_{yy}}$  value of 0.59 (Figure 2d dashed orange curve).

### 3.3 From system-size events to complex seismic sequences

The observed seismic sequences exhibited a wide range of behaviors, from regular complete ruptures to complex seismicity patterns, including partial events interspersed between consecutive complete ruptures. For each event (partial or complete), the rupture length was determined based on the fault segment that exhibited a sudden shear stress drop, a hallmark of rupture propagation (Figure 3a). The resolution of these mea-

measurements depends on the spatial arrangement of the strain gauges along the fault. Complete ruptures show a rupture length of 2 m.

Experiments carried out with the large stopper revealed the most diverse rupture size distribution, with an average of six partial ruptures occurring between two successive complete ruptures (Figure 3a). In contrast, experiments with the top-medium stopper yielded an average of two partial ruptures between consecutive complete ruptures. Experiments conducted with the bottom-medium stopper were predominantly characterized by system-size events, consisting of single complete ruptures occurring at regular intervals. The bottom-small stopper experiments exhibited a more complex distribution, with an average of four partial ruptures occurring between two complete ruptures. Finally, experiments involving the top-small stopper were largely dominated by periodic complete ruptures.

The patterns of inter-event times provide further insight into how the stress distribution influences the complexity of the seismic cycle. We define two distinct time intervals (Gualandi et al., 2023):  $T_{\text{pre}}$  is the time elapsed between a given event and the one preceding it, and  $T_{\text{next}}$  is the time between an event and the subsequent one. For events occurring periodically  $T_{\text{pre}} = T_{\text{next}}$ , while for events not occurring periodically  $T_{\text{pre}} \neq T_{\text{next}}$ . This analysis was performed for each external loading condition by considering (i) complete events only (Figure 3c) and (ii) all events, including both partial and complete ruptures (Figure 3c). The inter-event times between complete events show almost periodic behavior (with values ranging between 2 and 6 seconds, Figure 3d), regardless of the interspersed occurrence of partial ruptures. The only exception is an example of cycle skipping in experiment n19 (shown in blue in Figure 3), where the second expected complete rupture was instead a slow slip event, without the sharp and pronounced stress drop observed in fast rupture events (Figure S1). When considering the totality of events (Figure 3b), the inter-event times ranged between 0.1 and 1.5 seconds for the complex sequences (n26, n18, and n22) and between 2.1 and 3.5 seconds for the system-size sequences (n19, n23). Many of them, mostly partial ruptures, occur periodically (data points aligned near the 1 : 1 slope in Figure 3d; this happened for 70%, 21%, 50%, 42%, and 100% of the total number of events respectively for n26, n18, n19, n22, n23). Interestingly, the inter-event times of the remaining events, those that deviate from periodicity, tend to cluster along different slopes, suggesting that the fault behavior tends towards a periodic pattern. This is evident in Figure 3a for experiment n18, where the second, third, and fourth sequences follow a similar pattern: a longer interval after a complete rupture, followed by two shorter intervals after partial ruptures. Similarly, in experiment n22, both the second and third sequences exhibit an initial longer interval (following a complete rupture), followed by four shorter ones.

In this context, the inter-event time is governed by the static friction drop experienced by the preceding rupture at the nucleation site. Larger friction drops lead to longer inter-event times (Figure S2). Notably, the greater static friction drops associated with complete ruptures are influenced by post-seismic activity, such as secondary ruptures and wave reflections, which is absent or minimal in the case of partial ruptures. These processes further weaken the fault, resulting in a larger static stress drop. At the same time, they delay the fault's re-locking and subsequent re-loading. The magnitude of this effect depends on the stress distribution, leading to a range of  $\frac{T_{\text{next}}}{T_{\text{pre}}}$  values between 1 and 4.

## 4 Discussion

### 4.1 On the emergence of complex seismic cycles

The initial stress distribution controlled the nucleation location of the rupture events, which occurred at different positions along the fault. In particular, the nucleation loca-



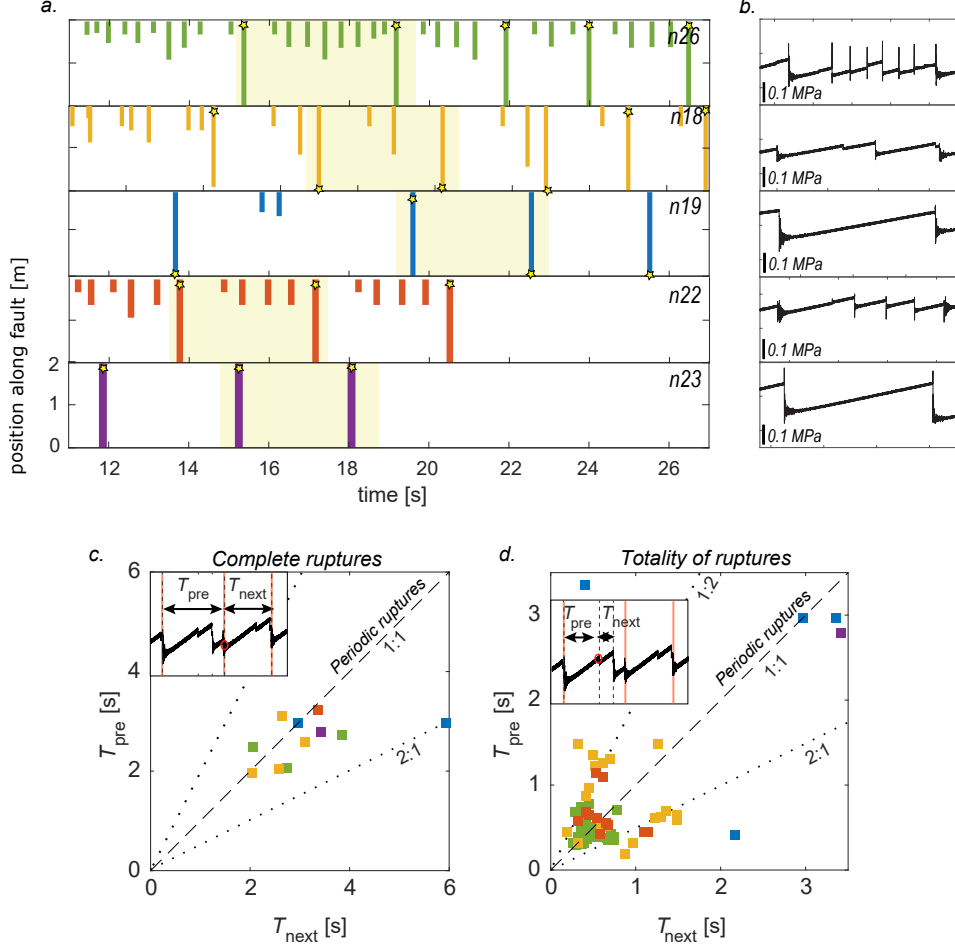


**Figure 3.** (a) Occurrence time and rupture length for all the events (partial and complete) in selected experiments (from top to bottom: n26, n18, n19, n22, n23). Because the precision of the rupture length estimates is constrained by the location of the sensors, complete ruptures breaking the whole 2.5 m-long fault appear here as 2 m long. Stars indicate the nucleation location of each complete rupture. (b) Shear stress evolution for each seismic sequence highlighted in yellow, measured by strain gauge SG7 ( $x=1.7$  m). Inter-event times computed (c) for complete ruptures only and (d) for all the events, partial and complete.  $T_{\text{pre}}$  is the time between one event and the one that precedes it, and  $T_{\text{next}}$  the time between that same event and the one that follows it. Color legend follows the one indicated in Figure 1.



tions were correlated with the local stress ratio  $\frac{\tau}{\sigma_{yy}}$ , and occurred consistently at the places where it was maximal. This observation is consistent with previous studies that highlight that rupture nucleation tends to occur where  $\frac{\tau}{\sigma_{yy}}$  is maximal (Ben-David & Fineberg, 2011). However, we also observed that the values of  $\frac{\tau}{\sigma_{yy}}$  at nucleation were not fixed but ranged between 0.35 and 0.6 (values sensitive to the spatial resolution of our measurements). So, while  $\frac{\tau}{\sigma_{yy}}$  plays a key role in controlling the onset of rupture, it is not a sufficient nucleation criterion. In fact, nucleation models show that other quantities can contribute significantly; for example, potential and fracture energies control nucleation through quasi-static crack growth in the large-scale yield regime (e.g. Rubin & Ampuero, 2005).

The heterogeneous stress distribution not only influences rupture nucleation but also shapes the overall seismic cycle. In particular, stress heterogeneity induces complexities in the seismic cycle, leading to the emergence of finite rupture events between complete ruptures. Importantly, despite the occurrence of these finite events, the recurrence time of complete ruptures remains unchanged in these experiments.

The seismicity statistics surrounding a major event are generally explained by the frictional properties of faults (Kaneko et al., 2010; Dublanchet et al., 2013; Wang et al., 2024) or geometrical characteristics (Dal Zilio et al., 2019), but even a single homogeneous fault can exhibit complex behavior if sufficiently long (Cattania, 2019). Our experiments integrate these conditions. The seismic cycles occurred on a single fault ( $L=2.5$  m) approximately 100 times larger than the expected nucleation length ( $L_c=2.5$  cm (Lattour et al., 2013; Paglialunga et al., 2023)). According to Cattania (2019), such a high  $\frac{L}{L_c}$  ratio is sufficient to induce the occurrence of sub-system-size events in the presence of a heterogeneous loading. More generally, the number of rupture events per cycle is expected to be a function of  $\frac{L}{L_c}$ , once accounted for the loading conditions and heterogeneous on-fault stress distribution.

In particular, the emergence of partial ruptures can be explained through an energetic perspective. In Linear Elastic Fracture Mechanics, rupture propagation occurs when the energy release rate ( $G$ ) at the rupture tip exceeds the fracture energy ( $G_c$ ), which resists rupture propagation. If the available energy is insufficient, the rupture will arrest. This can occur due to either a reduction in  $G$  or an increase in  $G_c$  (Figure S4). In our experimental seismic sequences, multiple ruptures sequentially arrested when the energy release rate fell below the fracture energy ( $G < G_c$ ). This arrest increased shear stress in the unruptured section of the fault (Figure S4c, Figure S5d), raising the energy available for subsequent ruptures (Figures S4d-e). Eventually, this process led to full rupture propagation once  $G$  exceeded  $G_c$  along the entire fault. This analysis aligns with rupture length predictions within the Linear Elastic Fracture Mechanics framework (Kammer et al., 2015; Bayart et al., 2016; Ke et al., 2018) (see supplementary material).

The temporal evolution of stress during the sequence shows that, as the shear stress approaches its critical distribution (bright green curve in Figure S4c), the local stress increase generated by the arrest of the previous partial rupture becomes progressively smaller. This process culminates in an almost imperceptible rise, which ultimately leads to a complete rupture. This phenomenon is also evident in Figure S3, where the stress distributions immediately before the complete rupture and before the preceding partial rupture overlap almost entirely. Moreover, not only does the stress distribution converge toward the critical state, but the partial events preceding a complete rupture exhibit similar propagation phases (Figure S3), as already observed in numerical studies (Lapusta & Rice, 2003). This behavior aligns with natural observations of similar initiation of small and large earthquakes (Meier et al., 2017). As the fault state approaches its critical conditions, predicting the timing of the main event becomes increasingly challenging.

Our experiments also provide valuable insight into interevent times. For complex sequences, when considering all events (both partial and complete), their occurrence is, at first glance, aperiodic, with inter-event times ranging from 0.1 to 3.3 seconds (Fig-

ure 3d). However, a closer examination reveals a tendency of the fault toward periodic patterns. In particular, most partial ruptures occur periodically, whereas complete ruptures often result in longer interevent times. This behavior is governed by the heterogeneous stress distribution along the fault, a behavior previously observed in experimental fault systems (Caniven et al., 2017). This phenomenon has also been employed as an indirect method for mapping seismic asperities in space (Wyss et al., 2000). In contrast, complete ruptures exhibit periodic recurrence, with inter-event times of 2 to 4 seconds (Figure 3c), regardless of the complexity of the seismic sequence. Moreover, cycles involving only system-size events (associated with lower stress heterogeneity) tend to have slightly longer average recurrence times compared to cycles with multiple ruptures (associated with higher stress heterogeneity). This finding is consistent with the simulations of Cattania & Segall (2021), which show that rough faults exhibit longer recurrence times than smooth ones, suggesting that fault properties and stress heterogeneity may exert similar effects on periodicity. Our observation of the periodicity of complete ruptures highlights that interseismic activity has little impact on the recurrence time or magnitude of major events but primarily prepares the fault for critical conditions, ultimately enabling major failures.

## 4.2 Influence of stress heterogeneity on rupture dynamics

As previously stated, the majority of complete ruptures observed in these experiments exhibit *complex* rupture processes (Figure 1e). During such events, the rupture generally nucleates near the leading edge and accelerates to a rupture speed of approximately  $0.5 C_s$ . After propagating over a distance of about 50 cm, the rupture significantly decelerates to transient velocities ranging from 650 m/s to 56 m/s, depending on the event, over a fault segment of 0.9 m. This slowdown occurs in a region where the stress intensity factor is lower than in the earlier portion of the fault (Figure S4d), corresponding to an area presenting a stress barrier. The transient propagation of the rupture within this low-stressed region is accompanied by a stress build-up (Figure 4) over a period defined as  $t_{\text{delay}}$ , highlighted in yellow in Figure 4. Following this delay, a new rupture is dynamically triggered, propagating at supershear velocities.

Interestingly, the duration of  $t_{\text{delay}}$  varies significantly across the different complex ruptures observed, spanning more than an order of magnitude, ranging from 1.4 to 18 ms (Figure 4). The duration  $t_{\text{delay}}$  appears to be controlled by the initial level of stress along the barrier, before the transient rupture propagation. Effectively, for each loading conditions,  $t_{\text{delay}}$  decreases linearly with  $\Delta\tau_{\text{delay}}$ , defined as  $\tau_{\text{arrest}} - \tau_{\text{res}}$ , with  $\tau_{\text{arrest}}$  the shear stress at the arrest location before the stress build-up caused by the transient rupture propagation, and  $\tau_{\text{res}}$  the residual stress level achieved along the fault after the transient rupture propagation. Large values of  $\Delta\tau_{\text{delay}}$  induce faster transient rupture velocities within the stress barrier, resulting in shorter  $t_{\text{delay}}$ . Note that  $\Delta\tau_{\text{delay}}$  serves as a direct proxy for the severity of the barrier. Large  $\Delta\tau_{\text{delay}}$  indicates an initial stress state close to the fault's frictional strength, while small  $\Delta\tau_{\text{delay}}$  suggests an initial state of stress far from the fault's frictional strength.

To gain a deeper understanding of these conditions, numerical simulations were performed using the spectral element software SEM2DPACK (Ampuero, 2012; Ampuero et al., 2024).

An exponential slip-weakening friction law was used and justified by previous experimental observations highlighting a continued shear stress weakening with slip (Paglialunga et al., 2024). The critical slip distance, the static and residual frictional strength, as well as the initial stress distribution were extrapolated from experimental observations (i.e., heterogeneous distribution, Figure S8). A low shear stress zone was imposed to reflect the observed stress drop barrier (Figure S7). This locally generated friction values lower than the residual strength, forcing the rupture to slow down or arrest. The nucleation

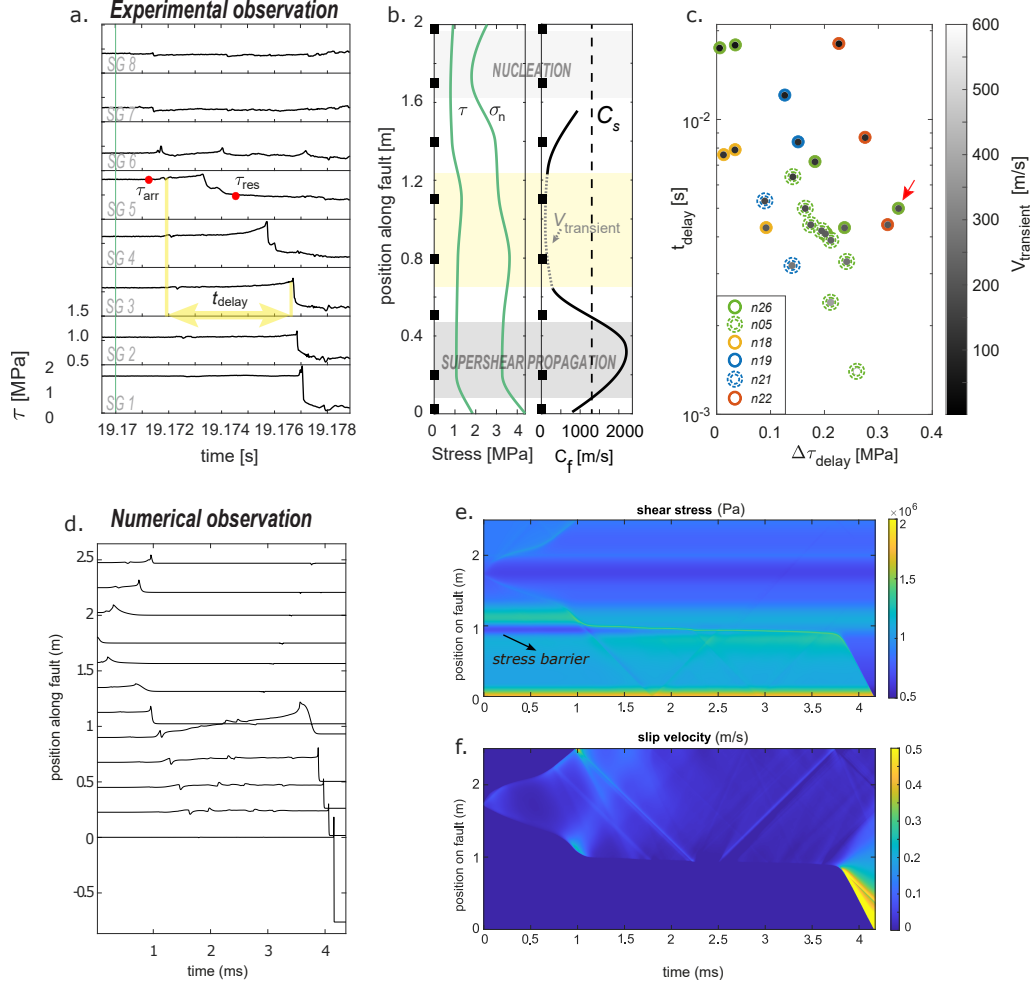


**Figure 4.** Top panels: Representative example of experimental observation of complex rupture. (a) Temporal evolution of shear stress for all strain gauge locations, with time delays highlighted in yellow. Red markers indicate values of  $\tau_{\text{arr}}$  and  $\tau_{\text{res}}$  used to compute  $\Delta\tau_{\text{delay}}$ . (b) The left panel shows the spatial distribution of normal and shear stress before the event (time indicated by the green line in panel a), and the right panel shows the rupture speed. (c) Delay times measured for all observed complex ruptures, with corresponding  $\Delta\tau_{\text{delay}}$ . A linear trend is observed within single experiments, suggesting that stress conditions control the time delay and triggering velocity. The red arrow indicates the event shown in (a). Bottom panels: Numerical observation of complex rupture. Details of the initial imposed stress and frictional parameters refer to Figure S8. (d) Temporal evolution of shear stress at equidistant fault locations. (e, f) Spatio-temporal evolution of slip velocity and shear stress.

was forced through a region of overstress imposed at  $x=1.76$  m, the same location as the experimental event.

The numerical simulations qualitatively reproduced the experimental observations, capturing a similar complex rupture propagation process (Figure 4). Upon nucleation, the rupture propagated bilaterally. The rightward-propagating front exhibited a variable subshear velocity until it reached the fault's edge. The leftward-propagating front initially traveled at a subshear velocity but briefly transitioned to supershear before encountering the stress drop barrier. At this point, the rupture decelerated abruptly, radiating stopping waves (Figure 4e) that reduced slip velocity in the wake of the rupture tip. Additionally, S-waves were radiated ahead of the rupture front (Figure 4f).

Within the stress drop barrier, the rupture did not fully arrest but instead propagated at a very low velocity. This creeping front was governed by continued weakening under the exponential slip-weakening law and was accompanied by a shear stress increase ahead of the rupture tip (Figure 4f, where the light blue area contrasts with the initial dark blue area indicating the barrier). Moreover, S-waves previously radiated by the rupture were reflected at the fault edges. Upon re-entering the barrier, these reflected waves locally enhanced slip through a step-like increase. This gradual yet persistent rise in stress enabled the rupture to overcome the stress drop barrier, eventually reaching a shear stress level sufficient to resume dynamic propagation (the temporal evolution of the stress distribution is shown in Figure S9).

This numerical simulation qualitatively replicates the conditions applied in the laboratory, providing valuable insights into the interpretation of the experimental observations. It underscores the significant influence of a stress barrier on rupture dynamics, which can markedly alter propagation behavior without necessarily stopping the rupture. This behavior arises when the governing friction law incorporates continued weakening, as demonstrated by the exponential slip-weakening law used in this study. In particular, continued slip-weakening has proven to be a highly effective mechanism to facilitate the advancement of the rupture front in the presence of a stress barrier (Paglialunga et al., 2022).

Interestingly, this process bears similarities to the observed creep fronts in laboratory experiments on analog materials containing quartz gouge faults (S. B. L. Cebry et al., 2022). However, in those experiments, delayed triggering was attributed to a combination of initial overstress and the frictional properties of the gouge. These observations collectively highlight how the transition from partial to complex events can be very abrupt. One could argue that these so-called complex ruptures correspond to two distinct seismic events. Notably, the time delay observed between the two propagation phases is one to two orders of magnitude larger than the early dynamic propagation phase. This result questions the definition of the rupture event itself, where the second propagation phase could be interpreted as an early aftershock or, if of comparable sizes, as a doublet earthquake (Sladen et al., 2010). In our simulation, the critical slip distance is, on average, four microns, much smaller than what we would expect for natural earthquakes. Increasing the size of the fault and the size of  $D_c$  would enhance both the propagation time and the time delay between subsequent rupture phases. Although the first is expected to increase linearly with the length of the rupture, assuming a comparable rupture velocity, the second is mainly controlled by the severity of the barrier, with respect to the energy release rate characterizing the given rupture. A deeper investigation of the mechanism controlling the overcoming of a stress barrier, and in particular of the relation between the time delay and the severity of the barrier, will be the subject of future work.

## 5 Conclusions

Our results demonstrate that heterogeneous initial stress conditions along a large experimental fault can shift the system from inducing system-size, periodic ruptures to exhibiting greater complexity in the seismic cycle. This complexity is evident in the oc-

388 currence of instabilities, in their nucleation location, size, and inter-event time. The only  
389 characteristic independent of the initial stress distribution is the recurrence time of the  
390 major events. This strengthens the idea that a detailed investigation of the spatial and  
391 temporal evolution of seismicity along natural fault systems could help elucidate the evo-  
392 lution of stress distribution. In addition, we show that local stress heterogeneity is piv-  
393 otal in the control of rupture dynamics. The observed phenomenon of 'complex rupture'  
394 (arrest, delay of the rupture, and re-nucleation) shares similarities with the natural oc-  
395 currence of foreshock activity. It may provide insights into why not all large events are  
396 preceded by foreshocks and why not all small to medium events lead to larger ones.

## Open Research Section

This section MUST contain a statement that describes where the data supporting the conclusions can be obtained. Data cannot be listed as "Available from authors" or stored solely in supporting information. Citations to archived data should be included in your reference list. Wiley will publish it as a separate section on the paper's page. Examples and complete information are here: [https://www.agu.org/Publish with AGU/Publish/Author Resources/Data for Authors](https://www.agu.org/Publish-with-AGU/Publish/Author-Resources/Data-for-Authors)

## Acknowledgments

F.P. and M.V. acknowledge support from the European Research Council Starting Grant project 757290-BEFINE. F.P. and F.P. acknowledge support from the European Research Council Starting Grant project HOPE 101041966.

## References

- Ampuero, J. P. (2012). Sem2dpack, a spectral element software for 2d seismic wave propagation and earthquake source dynamics, v2.3.8. *Zenodo*. doi: 10.5281/zenodo.230363
- Ampuero, J. P., Currie, T. W., Herrera, M. T., Huang, Y., Lestrelin, H., Liang, C., ... Weng, H. (2024). jpampuero/sem2dpack: Sem2dpack v2.3.9 (sem2dpack.2.3.9). *Zenodo*, [software]. doi: 10.5281/zenodo.13821494
- Bayart, E., Svetlizky, I., & Fineberg, J. (2016). Fracture mechanics determine the lengths of interface ruptures that mediate frictional motion. *Nature Physics*, 12(2), 166–170. doi: 10.1038/nphys3539
- Bayart, E., Svetlizky, I., & Fineberg, J. (2018). Rupture Dynamics of Heterogeneous Frictional Interfaces. *Journal of Geophysical Research: Solid Earth*, 123(5), 3828–3848. doi: 10.1002/2018JB015509
- Ben-David, O., & Fineberg, J. (2011). Static friction coefficient is not a material constant. *Physical Review Letters*, 106(25), 1–4. doi: 10.1103/PhysRevLett.106.254301
- Brace, W. F., & Byerlee, J. D. (1966). Stick-Slip as a Mechanism for Earthquakes. *Science*, 153(3739), 990–992. Retrieved from <https://science.sciencemag.org/content/153/3739/990> doi: 10.1126/science.153.3739.990
- Caniven, Y., Dominguez, S., Soliva, R., Peyret, M., Cattin, R., & Maerten, F. (2017). Relationships between along-fault heterogeneous normal stress and fault slip patterns during the seismic cycle: Insights from a strike-slip fault laboratory model. *Earth and Planetary Science Letters*, 480, 147–157.
- Cattania, C. (2019). Complex Earthquake Sequences On Simple Faults. *Geophysical Research Letters*, 46(17-18), 10384–10393. doi: 10.1029/2019GL083628
- Cattania, C., & Segall, P. (2021, 4). Precursory slow slip and foreshocks on rough faults. *Journal of Geophysical Research: Solid Earth*, 126. doi: 10.1029/2020JB020430
- Cebry, S. B., Sorhaindo, K., & McLaskey, G. C. (2023). Laboratory earthquake rupture interactions with a high normal stress bump. *Journal of Geophysical Research: Solid Earth*, 128(11), e2023JB027297.
- Cebry, S. B. L., Ke, C.-y., Shreedharan, S., Marone, C., Kammer, D. S., & Mclaskey, G. C. (2022). Creep fronts and complexity in laboratory earthquake sequences illuminate delayed earthquake triggering. *Nature Communications*, 1–9. doi: 10.1038/s41467-022-34397-0
- Corbi. (2024). Asperity size and neighboring segments can change the frictional response and fault slip behavior: Insights from laboratory experiments and numerical simulations. *Journal of Geophysical Research: Solid Earth*, 129(1), e2023JB026594.



- Dal Zilio, L., van Dinther, Y., Gerya, T., & Avouac, J. P. (2019). Bimodal seismicity in the Himalaya controlled by fault friction and geometry. *Nature Communications*, 10, 1–11. Retrieved from <http://dx.doi.org/10.1038/s41467-018-07874-8> doi: 10.1038/s41467-018-07874-8
- Das, S., & Aki, K. (1977). Fault plane with barriers: A versatile earthquake model. *Journal of Geophysical Research*, 82(36), 5658–5670. doi: 10.1029/jb082i036p05658
- Dieterich, J. H. (1978). Preseismic Fault Slip and Earthquake Prediction. *Journal of Geophysical Research*, 83(8), 3940–3948. doi: 10.1029/JB083iB08p03940
- Dieterich, J. H. (1981). Potential for Geophysical Experiments in Large Scale Tests. *Geophysical Research Letters*, 8(7), 653–656. doi: 10.1029/GL008i007p00653
- Dublanchet, P., Bernard, P., & Favreau, P. (2013). Interactions and triggering in a 3-D rate-and-state asperity model. *Journal of Geophysical Research : Solid Earth*, 118(April), 2225–2245. doi: 10.1002/jgrb.50187
- Fryer, B., Lebihain, M., Noël, C., Paglialunga, F., & Passelègue, F. (2024). The effect of stress barriers on unconventional-singularity-driven frictional rupture. *Journal of the Mechanics and Physics of Solids*, 193, 105876. Retrieved from <https://www.sciencedirect.com/science/article/pii/S0022509624003429> doi: <https://doi.org/10.1016/j.jmps.2024.105876>
- Gounon, A., Latour, S., Letort, J., & El Arem, S. (2022). Rupture Nucleation on a Periodically Heterogeneous Interface. *Geophysical Research Letters*, 49(20). doi: 10.1029/2021gl096816
- Gualandi, A., Faranda, D., Marone, C., Cocco, M., & Mengaldo, G. (2023, 2). Deterministic and stochastic chaos characterize laboratory earthquakes. *Earth and Planetary Science Letters*, 604. doi: 10.1016/j.epsl.2023.117995
- Guérin-Marthe, S., Nielsen, S., Bird, R., Giani, S., & Di Toro, G. (2019). Earthquake Nucleation Size: Evidence of Loading Rate Dependence in Laboratory Faults. *Journal of Geophysical Research: Solid Earth*, 124(1), 689–708. doi: 10.1029/2018JB016803
- Gvrtzman, S., & Fineberg, J. (2021). Nucleation fronts ignite the interface rupture that initiates frictional motion. *Nature Physics*, 17(9), 1037–1042.
- Iwashita, W., Matsukawa, H., & Otsuki, M. (2023). Static friction coefficient depends on the external pressure and block shape due to precursor slip. *Scientific Reports*, 13(1), 2511.
- Kammer, D. S., Radiguet, M., Ampuero, J. P., & Molinari, J. F. (2015). Linear elastic fracture mechanics predicts the propagation distance of frictional slip. *Tribology Letters*, 57(3). doi: 10.1007/s11249-014-0451-8
- Kaneko, Y., Avouac, J. P., & Lapusta, N. (2010). Towards inferring earthquake patterns from geodetic observations of interseismic coupling. *Nature Geoscience*, 3(5), 363–369. doi: 10.1038/ngeo843
- Ke, C. Y., McLaskey, G. C., & Kammer, D. S. (2018). Rupture Termination in Laboratory-Generated Earthquakes. *Geophysical Research Letters*, 45(23), 12,784–12,792. doi: 10.1029/2018GL080492
- Ke, C.-Y., McLaskey, G. C., & Kammer, D. S. (2020). The earthquake arrest zone. *Geophysical Journal International*, 224(1), 581–589. doi: 10.1093/gji/ggaa386
- Lapusta, N., & Rice, J. R. (2003). Nucleation and early seismic propagation of small and large events in a crustal earthquake model. *Journal of Geophysical Research*, 108, 1–18. doi: 10.1029/2001JB000793
- Latour, S., Schubnel, A., Nielsen, S., Madariaga, R., & Vinciguerra, S. (2013). Characterization of nucleation during laboratory earthquakes. *Geophysical Research Letters*, 40(19), 5064–5069. doi: 10.1002/grl.50974
- Lu, X., Lapusta, N., & Rosakis, A. J. (2007). Pulse-like and crack-like ruptures in experiments mimicking crustal earthquakes. *Proceedings of the National Academy of Sciences*, 104(48), 18931–18936.



- Mastella. (2022). Foamquake: A novel analog model mimicking megathrust seismic cycles. *Journal of Geophysical Research: Solid Earth*, 127(3), e2021JB022789.
- Mclasky, G. (2019). Earthquake Initiation From Laboratory Observations and Implications for Foreshocks. *Journal of Geophysical Research : Solid Earth*, 124(12), 882–904. doi: 10.1029/2019JB018363
- Mclasky, G., & Lockner, D. (2014). Preslip and cascade processes initiating laboratory stick slip. *Journal of Geophysical Research*, 119(8), 6323–6336. doi: 10.1002/2014JB011220
- Meier, M.-A., Ampuero, J., & Heaton, T. H. (2017). The hidden simplicity of subduction megathrust earthquakes. *Science*, 357(6357), 1277–1281.
- Okubo, P., & Dieterich, J. (1981). Fracture energy of stick-slip events in a large scale biaxial experiment. *Geophysical Research Letters*, 8(8), 887–890.
- Okubo, P., & Dieterich, J. (1984). Effects of physical fault properties on frictional instabilities produced on simulated faults. *Journal of Geophysical Research: Solid Earth*, 89(B7), 5817–5827. doi: 10.1029/JB089iB07p05817
- Paglialunga, F., Passelègue, F., Brantut, N., Barras, F., Lebihain, M., & Violay, M. (2022). On the scale dependence in the dynamics of frictional rupture : Constant fracture energy versus size-dependent breakdown work. *Earth and Planetary Science Letters*, 584. doi: 10.1016/j.epsl.2022.117442
- Paglialunga, F., Passelegue, F., Latour, S., Gounon, A., & Violay, M. (2023). Influence of viscous lubricant on nucleation and propagation of frictional ruptures. *Journal Of Geophysical Research-Solid Earth*, 128(4), e2022JB026090.
- Paglialunga, F., Passelègue, F., Lebihain, M., & Violay, M. (2024). Frictional weakening leads to unconventional singularities during dynamic rupture propagation. *Earth and Planetary Science Letters*, 626, 118550.
- Radiguet, M., Kammer, D. S., Gillet, P., & Molinari, J. F. (2013). Survival of heterogeneous stress distributions created by precursory slip at frictional interfaces. *Physical Review Letters*, 111(16), 1–5. doi: 10.1103/PhysRevLett.111.164302
- Radiguet, M., Kammer, D. S., & Molinari, J. F. (2015). The role of viscoelasticity on heterogeneous stress fields at frictional interfaces. *Mechanics of Materials*, 80(PB), 276–287. Retrieved from <http://dx.doi.org/10.1016/j.mechmat.2014.03.009> doi: 10.1016/j.mechmat.2014.03.009
- Rosakis, A. J., Samudrala, O., & Coker, D. (1999). Cracks faster than the shear wave speed. *Science*, 284(5418), 1337–1340. doi: 10.1126/science.284.5418.1337
- Rubin, A. M., & Ampuero, J. P. (2005). Earthquake nucleation on (aging) rate and state faults. *Journal of Geophysical Research*, 110(2), 1–24. doi: 10.1029/2005JB003686
- Rubino, V., Lapusta, N., & Rosakis, A. (2022a). Intermittent lab earthquakes in dynamically weakening fault gouge. *Nature*, 606(7916), 922–929.
- Rubino, V., Lapusta, N., & Rosakis, A. J. (2022b). Intermittent lab earthquakes in dynamically weakening fault gouge. *Nature*, 606(7916), 922–929. doi: 10.1038/s41586-022-04749-3
- Rubino, V., & Rosakis, A. (2020). Spatiotemporal properties of sub-rayleigh and supershear ruptures inferred from full-field dynamic imaging of laboratory experiments. *Journal of Geophysical Research: Solid Earth*, 125(2), e2019JB018922.
- Rubinstein, S. M., Barel, I., Reches, Z., Braun, O. M., Urbakh, M., & Fineberg, J. (2011). Slip sequences in laboratory experiments resulting from inhomogeneous shear as analogs of earthquakes associated with a fault edge. *Pure and Applied Geophysics*, 168, 2151–2166.
- Rubinstein, S. M., Cohen, G., & Fineberg, J. (2004). Detachment fronts and the onset of dynamic friction. *Nature*, 430(August), 1005–1009. doi: 10.1038/nature02861.1.
- Salditch, L., Stein, S., Neely, J., Spencer, B. D., Brooks, E. M., Agnon, A., & Liu, M. (2020). Earthquake supercycles and long-term fault memory. *Tectonophysics*,

774, 228289.

- Sladen, A. a., Tavera, H., Simons, M., Avouac, J.-P., Konca, A., Perfettini, H., ...  
Cavagnoud, R. (2010). Source model of the 2007 mw 8.0 pisco, peru earthquake:  
Implications for seismogenic behavior of subduction megathrusts. *Journal of  
Geophysical Research: Solid Earth*, 115(B2).
- Svetlizky, I., & Fineberg, J. (2014). Classical shear cracks drive the onset of dry fric-  
tional motion. *Nature*, 509(7499), 205–208. doi: 10.1038/nature13202
- Svetlizky, I., Kammer, D., Bayart, E., Cohen, G., & Fineberg, J. (2017, mar).  
Brittle Fracture Theory Predicts the Equation of Motion of Frictional Rup-  
ture Fronts. *Physical Review Letters*, 118(12), 125501. Retrieved from  
<https://link.aps.org/doi/10.1103/PhysRevLett.118.125501> doi:  
10.1103/PhysRevLett.118.125501
- Tal, Y., Rubino, V., Rosakis, A. J., & Lapusta, N. (2022). Dynamics and near-field  
surface motions of transitioned supershear laboratory earthquakes in thrust faults.  
*Journal of Geophysical Research: Solid Earth*, 127(3), e2021JB023733.
- Tinti, E., Spudich, P., & Cocco, M. (2005). Earthquake fracture energy inferred  
from kinematic rupture models on extended faults. *Journal of Geophysical Re-  
search: Solid Earth*, 110(12), 1–25. doi: 10.1029/2005JB003644
- Wang, L., Xu, S., Zhuo, Y., Liu, P., & Ma, S. (2024, 6). Unraveling the roles of fault  
asperities over earthquake cycles. *Earth and Planetary Science Letters*, 636. doi:  
10.1016/j.epsl.2024.118711
- Wyss, M., Schorlemmer, D., & Wiemer, S. (2000, 4). Mapping asperities by min-  
ima of local recurrence time: San jacinto-elsinore fault zones. *Journal of Geophys-  
ical Research: Solid Earth*, 105, 7829–7844. doi: 10.1029/1999jb900347
- Xia, K., Rosakis, A. J., & Kanamori, H. (2004). Laboratory earthquakes: The sub-  
rayleigh-to-supershear rupture transition. *Science*, 303(5665), 1859–1861.
- Yamashita, F., Fukuyama, E., Xu, S., Kawakata, H., Mizoguchi, K., & Takizawa,  
S. (2021a). Two end-member earthquake preparations illuminated by foreshock  
activity on a meter-scale laboratory fault. *Nature Communications*, 12(1), 4302.
- Yamashita, F., Fukuyama, E., Xu, S., Kawakata, H., Mizoguchi, K., & Takizawa,  
S. (2021b). Two end-member earthquake preparations illuminated by foreshock  
activity on a meter-scale laboratory fault. *Nature Communications*, 12(1), 1–  
11. Retrieved from <http://dx.doi.org/10.1038/s41467-021-24625-4> doi:  
10.1038/s41467-021-24625-4
- Yamashita, F., Fukuyama, E., Xu, S., Mizoguchi, K., Kawakata, H., & Takizawa,  
S. (2018). Rupture preparation process controlled by surface roughness on  
meter-scale laboratory fault. *Tectonophysics*, 733(September 2017), 193–  
208. Retrieved from <https://doi.org/10.1016/j.tecto.2018.01.034> doi:  
10.1016/j.tecto.2018.01.034